

Biomechanics and Modeling in Mechanobiology

Estimating Passive Mechanical Properties in a Myocardial Infarction using MRI and Finite Element Simulations

--Manuscript Draft--

Manuscript Number:	BMMB-D-14-00088
Full Title:	Estimating Passive Mechanical Properties in a Myocardial Infarction using MRI and Finite Element Simulations
Article Type:	Original Research
Keywords:	Myocardial Infarction; Finite Element Modeling; Left Ventricular Remodeling; MRI; Optimization
Abstract:	<p>Myocardial infarction (MI) triggers a series of maladaptive events that lead to structural and functional changes in the left ventricle. It is crucial to better understand the progression of adverse remodeling, in order develop effective treatment. In addition, being able to assess changes in-vivo would be a powerful tool in the clinic. The goal of the current study is to quantify the in-vivo material properties of infarcted and remote myocardium 1 week after MI, as well as the orientation of collagen fibers in the infarct. This will be accomplished by using a combination of magnetic resonance imaging (MRI), catheterization, finite element modeling, and numerical optimization to analyze a porcine model (N=4) of posterolateral myocardial infarction. Specifically, properties will be determined by minimizing the difference between in-vivo strains and volume calculated from MRI and finite element model predicted strains and volume. The results indicate that the infarct region is stiffer than the remote region, and that the infarct collagen fibers become more circumferentially oriented 1 week post-MI. These findings are consistent with previous studies, which employed ex-vivo techniques. The proposed methodology will ultimately provide a means of predicting remote and infarct mechanical properties in-vivo at any time point post-MI.</p>

Estimating Passive Mechanical Properties in a Myocardial Infarction using MRI and Finite Element Simulations

Dimitri Mojsejenko¹
Jeremy R. McGarvey²
Shauna M. Dorsey³
Joseph H. Gorman, III²
Jason A. Burdick³
James J. Pilla^{2,4}
Robert C. Gorman²
Jonathan F. Wenk^{1,5*}

Department of Mechanical Engineering¹ University of Kentucky, Lexington, KY;
Gorman Cardiovascular Research Group and Department of Surgery² University of Pennsylvania, Philadelphia, PA;
Department of Bioengineering³ University of Pennsylvania, Philadelphia, PA;
Department of Radiology⁴ University of Pennsylvania, Philadelphia, PA;
Department of Surgery⁵ University of Kentucky, Lexington, KY

Submitted to: Biomechanics and Modeling in Mechanobiology
Article Type: Original Research

*Co-Corresponding Author:
Jonathan F. Wenk, Ph.D.
University of Kentucky
Department of Mechanical Engineering
269 Ralph G. Anderson Building
Lexington, KY 40506-0503
Phone: (859) 218-0658
Fax: (859) 257-3304
Email: wenk@engr.uky.edu

Abstract

Myocardial infarction (MI) triggers a series of maladaptive events that lead to structural and functional changes in the left ventricle. It is crucial to better understand the progression of adverse remodeling, in order develop effective treatment. In addition, being able to assess changes in-vivo would be a powerful tool in the clinic. The goal of the current study is to quantify the in-vivo material properties of infarcted and remote myocardium 1 week after MI, as well as the orientation of collagen fibers in the infarct. This will be accomplished by using a combination of magnetic resonance imaging (MRI), catheterization, finite element modeling, and numerical optimization to analyze a porcine model (N=4) of posterolateral myocardial infarction. Specifically, properties will be determined by minimizing the difference between in-vivo strains and volume calculated from MRI and finite element model predicted strains and volume. The results indicate that the infarct region is stiffer than the remote region, and that the infarct collagen fibers become more circumferentially oriented 1 week post-MI. These findings are consistent with previous studies, which employed ex-vivo techniques. The proposed methodology will ultimately provide a means of predicting remote and infarct mechanical properties in-vivo at any time point post-MI.

Key Terms: Myocardial Infarction, Finite Element Modeling, Left Ventricular Remodeling, MRI, Optimization

1. Introduction

Nearly 8 million Americans have suffered a myocardial infarction (MI), with over 700,000 additional MI's occurring each year (Go et al. 2014). Left ventricular (LV) remodeling is the maladaptive structural and functional sequelae of MI that leads to symptomatic heart failure. Infarct expansion (i.e. stretching) has been identified as the initiating and sustaining phenomenon that drives adverse LV remodeling after MI (Jackson et al. 2002). In spite of the importance of infarct material properties on infarct expansion, little data exists on the time-dependent changes in this critical parameter during the remodeling process. Such data is crucial to a full understanding of MI-induced LV remodeling as well as for the development of new and more effective therapies to treat and/or prevent the development of heart failure after MI.

There have been a number of experimental studies that have sought to characterize the structural and functional changes that occur at discrete time points after the induction of MI. Holmes et al. (Holmes et al. 1997) investigated the collagen content and strain patterns in isolated pig hearts 3 weeks after a lateral wall infarct was induced. In that study, markers were embedded transmurally through the LV wall, allowing for strain to be calculated during passive inflation. It was found that the circumferential component of strain decreased significantly, indicating increased stiffness along that direction. Histological examination found significant collagen deposition in the MI. In addition, the collagen fibers were highly aligned and oriented within 30 degrees of the circumferential axis. In a similar study, Fomovsky et al. (Fomovsky et al. 2012) evaluated the collagen structure in rats which had undergone either apical or anterior wall infarction. In both cases, collagen content increased due to infarction. However, collagen fibers in the anterior wall infarcts tended to align with the circumferential axis, while the apical

infarcts had more randomly distributed fibers. These results indicate that the location of the infarct plays a crucial role in the structure of the collagen fibers.

Few studies have been conducted that experimentally quantify the stiffness of infarcted tissue by means of mechanical testing. Gupta et al. (Gupta et al. 1994) investigated the stiffness of anteroapical aneurysms in sheep over a 6 week period. Equibiaxial stretch testing was performed on infarcted and remote tissue within 4 hours of MI induction, as well as 1, 2, and 6 weeks post-MI. The results showed a significant increase in stiffness leading up to the 2 week mark, and then showed a significant decrease in stiffness at 6 weeks. Morita et al. (Morita et al. 2011) performed equibiaxial testing of infarcted tissue from control and treated sheep 8 weeks after anteroapical infarction. At that time point, the infarct stiffness was isotropic in the control case, but showed increased longitudinal stiffness in the treated case. Zhang et al. (Zhang et al. 2010) performed diffusion tensor magnetic resonance imaging (DTMRI) and equibiaxial testing on pig hearts 2 days after infarction. In this study, infarcts were generated in the lateral wall and apex of the LV, as well as in the lateral wall of the RV. The biaxial stress-stretch curves show anisotropic stiffness in the lateral wall infarcts and isotropic stiffness in the apical infarct. The results of the imaging study indicate that myofibers are not detectable within the infarcted region using DTMRI. In general, DTMRI is currently unable to quantify collagen fiber orientation within the MI, due to the manner in which water diffuses within this region. Thus histology is still required to assess these fiber angles post infarction.

Techniques have been developed that use a combination of magnetic resonance imaging (MRI), catheterization, and finite element modeling in order to estimate in-vivo myocardial material properties in a non-invasive manner. In all of these studies, the finite element models were based on anatomically correct geometry, which was contoured from MRI data. Moulton et

al. (Moulton et al. 1996) used 2D tagged MRI, finite element models with an isotropic material law and linearized strain, and a Levenberg-Marquardt optimization method to estimate the passive material properties of the healthy canine heart. This work utilized a single short axis slice to determine in-plane strains and compare them to a 2D finite element model. Wang et al. (Wang et al. 2009) used 3D tagged MRI, nonlinear finite element modeling, and a sequential quadratic programming optimization method to estimate passive properties in a single canine heart. The material parameters were fitted to a transversely-isotropic hyperelastic constitutive law (Guccione et al. 1991). Fiber architecture from diffusion tensor imaging was incorporated into the finite element models, rather than using histological data. Recently, Xi et al. (Xi et al. 2013) used 3D tagged MRI, nonlinear finite element modeling, and the method of parameter sweeps to estimate passive properties in a healthy human ventricle and two diseased human ventricles. In that study, the Guccione transversely-isotropic hyperelastic constitutive law was also employed (Guccione et al. 1991), but the fiber angles were assigned to vary from -60 degrees at the epicardium to 60 degrees at the endocardium based on histological data. The results indicated that myocardial stiffness increased in the diseased cases. Sun et al. (Sun et al. 2009) used 3D tagged MRI, nonlinear finite element modeling, and a successive response surface methodology to estimate active material properties in the remote and border zone regions of sheep ventricles with anteroapical aneurysm 8 weeks post-MI. This same approach was employed by Wenk et al. (Wenk et al. 2011) to evaluate active properties in the remote region and border zone of sheep ventricles with posterobasal infarction. In both of these studies, the border zone contractility was found to be depressed, relative to the remote region.

Other work has been done to assess the passive material properties in isolated hearts. Okamoto et al. (Okamoto et al. 2000) used 3D tagged MRI and finite element modeling to

estimate myocardial properties in isolated arrested canine hearts. In this work, an experimental suction apparatus was attached to the epicardial wall in order to generate deformations with shear strains. Augenstein et al. (Augenstein et al. 2006) used SPAMM (SPAtial Modulation of Magnetization) MRI, catheterization, and 3D finite element modeling to estimate the material properties in arrested pig hearts that underwent passive inflation. Unlike previous studies, fiber architecture from diffusion tensor imaging was incorporated into the finite element models, rather than using histological data. Nair et al. (Nair et al. 2007) used previously measured epicardial strain at 2 points on the surface of an isolated rabbit heart, along with a 3D finite element model, to estimate material parameters. The number of strain points used did not yield much information about myocardial deformation. However, the focus of this work was to present the use of a genetic algorithm optimization scheme for estimating material parameters.

Each of the aforementioned in-vivo and isolated heart studies focused on determining properties only in viable myocardium. To our knowledge, no such studies have determined the in-vivo passive material properties of a myocardial infarction. The goal of the current study is to quantify the in-vivo material properties of infarcted and remote myocardium in a porcine model 1 week after MI, as well as the orientation of collagen fibers in the infarcted zone, rather than assigning them a priori. This will be accomplished by using a combination of MRI, catheterization, and finite element modeling. Properties will be determined by using an optimization scheme to minimize the difference between in-vivo strains and volume calculated from MRI and finite element model predicted strains and volume. This investigation will ultimately provide a means of predicting remote and infarct mechanical properties at any time point post-MI.

2. Methods

2.1. Animal Model of MI

The animals used in this work received care in compliance with the protocols approved by the Institutional Animal Care and Use Committee at the University of Pennsylvania in accordance with the guidelines for humane care (National Institutes of Health Publication 85-23, revised 1996).

Myocardial infarction was induced in adult male Yorkshire swine (N=4) weighing approximately 40 kg. The pigs were anesthetized and the LV free wall exposed through a left thoracotomy. A posterior MI was induced by suture ligation of the left circumflex artery (LCX) and select obtuse marginal (OM) branches. An example of the ligation points for one of the cases is shown in Figure 1. In general, this ligation approach produced an infarct comprising 20-25% of the left ventricle. Ten MRI-compatible platinum wire markers were sutured to the epicardium around the infarct periphery immediately following infarction to enable infarct contouring from subsequent MRI acquisitions.

2.2. MRI Acquisition and Image Analysis

Cardiac MRI was performed 1 week post-MI using a 3T Seimens Trio A Tim Magnetom scanner (Seimens; Malvern, PA). For each MRI scan, a high fidelity pressure transducer (Millar Instruments; Houston, TX) was guided into the LV for cardiac gating. The measured pressure was later used to load the FE model (Figure 2). Images were collected using two techniques: 1) 3D SPAMM was performed in order to assess regional wall strain and 2) late-gadolinium enhanced (LGE) images were taken to further define the infarct area (Figure 3). The endocardium and epicardium of the LV were contoured from the 3D SPAMM images using ImageJ software (NIH; Bethesda, MD). The reference contours were generated at early diastolic

filling (Figure 3), following isovolumic relaxation, in order to generate the animal-specific ventricular geometry. Additionally, the endocardium was contoured at end-diastole in order to calculate LV volume. Infarct boundaries were created by identifying the platinum epicardial markers in the 3D SPAMM images. The total infarct area was confirmed by comparing marker positions with the enhanced region in the LGE images. Diastolic strain was calculated from the 3D SPAMM images using a custom optical flow plug-in for ImageJ to derive 3D displacement flow fields (Xu et al. 2010). It should be noted that the LV strain, volume, and contour data were all generated from the 3D SPAMM images and matched with simultaneous pressure measurements. This ensures continuity between all data used to generate the model.

2.3. FE Model Generation

The reference state for the FE model was taken to be at early diastole, where LV pressure is at a minimum and is therefore closest to an in-vivo stress-free state. Each set of endocardial and epicardial reference contours were fit with 3D surfaces to represent the animal-specific geometry (Rapidform; INUS Technology, Inc., Sunnyvale, CA). The boundary between the infarct and remote region was defined using 3D spline curves that were created by visually tracing infarct marker positions from MR images and then projecting onto the endocardial and epicardial surfaces. The FE mesh was produced by filling the volume between endocardial and epicardial surfaces with hexahedral brick elements incorporating a trilinear interpolation scheme (TrueGrid; XYZ Scientific, Inc., Livermore, CA, USA). The wall of each FE model consisted of 3 elements transmurally, 36 elements circumferentially, and 12 elements longitudinally, with a patch of 192 elements at the apex. A transmural thickness of three elements deep was previously found to be sufficient for accurate volume calculations while maintaining computational efficiency (Sun et al. 2009). The infarct and remote regions were designated as two separate materials, allowing for

different properties to be assigned to each (Figure 4). The inner endocardial surface was lined with linearly elastic shell elements to create an enclosed airbag for computing left ventricle cavity volume. The airbag had no influence on the mechanical response of the myocardium, as it was modeled as extremely soft with a Young's modulus of 1×10^{-10} kPa and Poisson's ratio of 0.3. Myofiber angles were assigned to each hexahedral element using a custom MATLAB script. The angles were appointed at the endocardial and epicardial surfaces and varied linearly through the transmural thickness. For the remote region, angles were fixed at -37 degrees at the epicardium and 83 degrees at the endocardium, with respect to the circumferential direction, based on previous studies with porcine ventricles (Hooks et al. 2007; Lee et al. 2012). The fiber angles in the infarct region were parameterized as part of the optimization, which will be discussed in a later section. Boundary conditions were implemented at the base of the LV to fully constrain displacement on the epicardial-basal edge, while allowing the remaining basal nodes to move in the circumferential-radial plane. The endocardial wall was loaded with a pressure boundary condition, which was based on the time course of the measured animal-specific diastolic pressure.

2.4. Constitutive model

The material response of the myocardium was assumed to be nearly incompressible, transversely isotropic, and hyperelastic. The diastolic mechanics are described by the strain energy function for passive myocardium developed by Guccione et al. (Guccione et al. 1991), in which a Fung-type exponential relation is used

$$W = \frac{1}{2} C (e^Q - 1), \quad (1)$$

with transverse-isotropy given by

$$Q = b_f E_{11}^2 + b_t (E_{22}^2 + E_{33}^2 + E_{23}^2 + E_{32}^2) + b_{fs} (E_{12}^2 + E_{21}^2 + E_{13}^2 + E_{31}^2). \quad (2)$$

The constants C , b_f , b_t , b_{fs} , are diastolic myocardial material parameters, E_{11} is the Green-Lagrange strain in the fiber direction, E_{22} is the cross-fiber in-plane strain, E_{33} is the radial strain transverse to the fiber direction, and the rest are shear strains. This strain energy function was used to describe both the remote and infarct regions, and was implemented through the use of a material subroutine in the FE solver LS-DYNA (Livermore Software Technology Corporation, Livermore, CA, USA).

2.5. Optimization

A genetic algorithm (GA) technique was chosen for the optimization, due to the large number of parameters to be optimized, and was performed using the software LS-OPT (Livermore Software Technology Corporation, Livermore, CA). Genetic algorithms perform well as global optimizers, whereas gradient-based methods can get stuck in local optima when exploring a large parameter space (LSTC manual). In a study by Nair et al. (Nair et al. 2007) GAs were found to be a robust method for optimizing cardiac material parameters in 3D models.

A total of 10 parameters were optimized in the current study. These included the diastolic material parameters from the strain energy function (C, b_f, b_t, b_{fs}) for both the remote and infarct regions, as well as the epicardial and endocardial fiber angles in the infarct. For the infarct, the fiber angles were assumed to vary linearly, as in the remote region. The ranges that were defined for each parameter are given in Table 1. These values were found to provide sufficient space for the optimization to converge without the bounds driving the solution.

The objective function that was minimized during the optimization was taken to be the mean squared error (MSE) between experimentally measured and FE predicted strains at an array of points in the midwall of the LV. Specifically, the centroids of midwall elements were compared to the nearest LV points from the MRI data where strain was measured. This was possible

because the LV contours used to generate the FE model and experimental strain points were from the same 3D SPAMM data. A total of seven rings of elements starting from the base, excluding the first ring, were used for the strain comparison. This led to a total of 252 points where strain was compared. Additionally the difference in LV cavity volume was added to the objective function and carried an equal weight as that of the strain points. The MSE was defined as

$$\text{MSE} = \sum_{n=1}^N \sum_{\substack{i=1,2,3; \\ j=1,2,3;}} w_n \left(E_{ij,n} - \bar{E}_{ij,n} \right)^2 + \sum_{m=1}^M w_m \left(\frac{V_m - \bar{V}_m}{\bar{V}_m} \right)^2 \quad (3)$$

where n is the strain point, N is the total number of strain points, $E_{ij,n}$ is the computed FE end-diastolic strain at each point, and V_m is the computed FE end-diastolic LV volume. The overbar represents animal-specific *in-vivo* measurements. An additional constraint was placed on the volume to ensure that it stayed bounded within $\pm 5\%$ of the experimentally measured volume.

A flowchart of the optimization process can be found in Figure 5. Briefly, the process begins with the generation of an initial population of 100 random designs. A “design” is a unique combination of the 10 parameters within each respective range, which are assigned to the FE model. After some initial testing, it was found that the population size of 100 FE simulations over 30 generations (iterations) allowed the genetic algorithm to produce consistently optimized results. After the initialization, a custom MATLAB script takes the fiber angles and modifies the fiber architecture of the FE model for each of the 100 designs. LS-DYNA then runs the FE simulations for each model, after which LS-OPT begins the optimization process (Stander et al. 2012). The designs are analyzed using the objective function defined previously. The 2 designs with the lowest MSE are saved for the next generation in a process called elitism. A tournament selection was chosen as the reproduction operator; in accordance, two individual designs are

randomly selected and the one with the lowest MSE is chosen to participate in mating. The designs of the next generation, the children, are created through an exploration operator referred to as crossover. This operator randomly selects a number of parents to mate to produce a number of children. The children carry qualities of each of their parents in the sense that their parameter values are the same as that of a parent or somewhere between the ranges of the parents. Using the standard (2,2) strategy for crossover, two children are created by and replace two parents. Therefore the sole victor decided in the tournament selection mates with each of the other 99 designs in the generation. Mutation is also involved in the creation of the child population and incites random changes in parameters based on a designated mutation probability. Once the child population of 100 is created, the 2 with the highest MSE are replaced by the 2 elites saved from the parent population. Hence the new generation is fully created and the process continues with the creation of the next set of models and simulations.

2.6. Simulated Equi-biaxial Extension

In order to facilitate a clearer interpretation of the material parameters, equi-biaxial extension tests were simulated using the parameters determined from the optimization. The constitutive law, given in Eqn. (1) and (2), was formulated for the case of planar equi-biaxial extension, as shown in Guccione et al. (Guccione et al. 1991). The resulting stress-strain equations were implemented into an in-house MATLAB script, where stress was calculated at the same set of strain points for each case. In the formulation, the fiber and cross-fiber directions were assumed to align with the loading directions. Additionally, the simulated sample was assumed to be a thin, incompressible segment of tissue in which there were no changes in fiber orientation through the thickness.

3. Results

Each of the 4 cases converged to an optimal set of material parameters before reaching 30 generations. Figure 6 shows an example of the design points generated in the optimization run for case 4. It can be seen in Figure 6a that the GA systematically searched the full parameter space, which was bounded by the range set at the beginning of the optimization. Note that the designs from early generations are evenly distributed throughout the parameter space, but that later generations begin to cluster around the optimal solution. Figure 6b shows a close-up of the convergence of parameter $b_{f,infarct}$. Note that a cluster forms over the final value of $b_{f,infarct}$ and that later generations have lower MSE values compared to earlier generations. Figure 7 shows how the best design found at each generation changes over the course of the optimization for case 2. The values of the non-angle parameters were normalized by their respective parameter ranges given in Table . Note that after generation 24 the parameter values do not change, indicating that the GA has converged to the optimal solution. All 4 of the cases converged with the same trends presented in the representative examples.

The optimized parameters for each of the 4 cases are given in Table 2. On average, the exponential parameters (b_f , b_t , b_{fs}) were found to be greater for the infarct region than the remote region. However, the average value of the C parameter was greater for the remote region, compared to the infarct region. The collagen fiber orientation at both the endocardium and epicardium became more circumferential in the infarct region, compared to the myofiber orientation in the remote region. Additionally, the MSE values ranged from 4.28 to 11.62 and are comparable to MSE values achieved in previous studies that employed a similar approach (Sun et al. 2009; Wenk et al. 2011). In fact, the current approach used 1.5 to 2 times more strain

components in the MSE calculation than the previous studies. This implies that the agreement, between the experimentally measured and FE predicted quantities, is better in the current work.

The results of the simulated equi-biaxial extension tests for all of the cases are shown in Figure 8a and 8b. It can be seen that there is variability between each of the cases, with case 4 showing the highest stiffness in both the remote and infarct region. In order to give a general comparison of stiffness in the remote and infarct regions, the stress-strain curves for all of the cases were averaged in each region. It can be seen in Figure 9 that the infarct region is stiffer than the remote region. Additionally, there appears to be more anisotropy in the infarct region compared to the remote region.

4. Discussion

The goal of the current study was to quantify the in-vivo passive material properties of infarcted and remote myocardium 1 week after MI using a combination of MRI, catheterization, FE modeling, and numerical optimization. To our knowledge, no previous studies have predicted the in-vivo passive material properties, or the collagen fiber orientation, in a myocardial infarction. The results of the current study indicate that the infarct region is stiffer than the remote region, and that the infarct collagen fibers become more circumferentially oriented 1 week post-MI. These findings are consistent with previous studies, which employed ex-vivo techniques.

The infarct collagen fiber architecture predicted in the current study indicates that both the epicardial and endocardial angles become more circumferentially oriented at 1 week after a posterolateral MI, compared to myofiber angles in the remote region. The endocardial angle shifted from 83 degrees to approximately 43 degrees, while the epicardial angle shifted from -37 degrees to approximately -18 degrees, a difference of 40 degrees and 19 degrees, respectively.

This result agrees with findings reported by Holmes et al. (Holmes et al. 1997) that showed a change in endocardial collagen angles of roughly 32 degrees towards the circumferential direction in pigs 3 weeks after a posterolateral MI, compared to sham controls. In addition, Rouillard and Holmes (Rouillard et al. 2012) reported a change of nearly 40 degrees towards the circumferential direction in both the endocardial and epicardial collagen fiber angles in rats 3 weeks post-MI. While there is little data in the literature regarding changes in collagen fiber orientation due to MI, the general trend is that fibers become more circumferential over time as the MI remodels (Holmes et al. 2005) when the infarct is located away from the LV apex.

The stiffness in the infarct region was found to be greater than the remote myocardium. This can be inferred when comparing the exponential parameter values for the infarct region to those for the remote (Table 2). However, it is easier to visualize the change in stiffness and anisotropy by using simulated equibiaxial stress-strain curves, as shown in Figure 9. Though few studies have performed experimental biaxial testing on infarcted tissue, Gupta et al. (Gupta et al. 1994) showed that the stiffness of apical aneurysms was greater than the remote myocardium in sheep 1 week post infarction. In addition, Zhang et al. (Zhang et al. 2010) performed biaxial testing on infarcted tissue from the lateral wall of pig ventricles 2 days post-MI. Those results showed increased extensibility in the cross-fiber direction, which was attributed to fiber disruption and necrosis that occurs within the first few days post-MI. The current results show much greater stiffness in both the fiber and cross-fiber directions at 1 week post-MI, which are consistent with the timeline of infarct remodeling outlined by Holmes et al. (Holmes et al. 2005).

The material parameters determined in the current study, in both the remote and infarct regions, showed variability from case to case (Table 2). However, this type of variability was seen in several previous studies of normal myocardium, where the values of C , b_f , b_t , and b_{fs}

varied by as much as a factor of 5 within the same group of animals (Okamoto et al. 2000; Walker et al. 2005; Augenstein et al. 2006). In general, the material parameters determined for the remote region in the current study were stiffer than those found in previous studies of normal myocardium (Guccione et al. 1991; Augenstein et al. 2005; Wang et al. 2009; Kichula et al. 2013). Since remodeling also takes place in the remote myocardium, this could alter the stiffness as the MI progresses. To our knowledge, no other studies have sought to quantify the material parameters in a posterolateral infarct by fitting a constitutive model with experimental data. Wenk et al. (Wenk et al. 2010) modeled a sheep LV with a posterobasal infarct that was 10 times stiffer than the remote region. This value was based on data reported from apical aneurysms and was imposed by scaling the C parameter, which stiffened all directions by the same amount. However, the current results show that anisotropy changes due to infarction (Figure 9).

Due to the nature of the constitutive equation, there are coupled interactions between the material coefficients. In particular, the parameter C affects stiffness in all directions, since it scales the stress in an isotropic manner. This issue has been addressed in previous studies, where MRI, finite element methods, and optimization were used to estimate passive myocardial properties. In work by Wang et al. (Wang et al. 2009) the optimization routine was designed to first determine C and then sequentially determine the remaining exponential parameters. In work by Xi et al. (Xi et al. 2013) the value of C was fixed to be 1 kPa, based on average values reported in other studies, which allowed the remaining parameters to be optimized independent of C. In the current work, the C parameters for both the remote and infarct regions were included as part of the design variables to be determined by the genetic algorithm. It was found that both C parameters converged to their final value after 10 iterations and remained steady as the other parameters continued to be optimized (Figure 7). This trend occurred in all 4 cases that were run

for this study, which implies that the genetic algorithm consistently determined the C parameter before the others. Another trend that was consistent between all 4 cases was that the remaining parameters converged to their final value by the 24th iteration (Figure 7). Thus, the final optimal set of parameters was fully determined well before the optimization terminated, leading to a steady MSE value for the final 7 iterations.

There are similarities and differences between the approach in the current study and previous work. MRI and catheterization were used to quantify wall motion and ventricular pressure, respectively, in both the current and previous studies (Sun et al. 2009; Wang et al. 2009; Wenk et al. 2011; Xi et al. 2013). In every case, finite element models were generated from the MRI-based geometry and loaded with the measured pressure, in order to simulate ventricular deformation. However, in work by Wang et al. (Wang et al. 2009) and Xi et al. (Xi et al. 2013) wall displacement was used in the optimization, whereas in the current study, and in work by Sun et al. (Sun et al. 2009) and Wenk et al. (Wenk et al. 2011), strain was used to quantify wall deformation in the optimization. Since displacement is the primary value measured by MRI and strain quantifies only deformation without rigid motion, each approach has distinct advantages.

There are several limitations associated with the approach presented in this work. In the current study, and the study by Xi et al. (Xi et al. 2013), average myofiber angles were assigned to the myocardium, which does not fully represent the spatially varying fiber architecture. In the future, fiber angles will be based on DTMRI data, similar to the study by Wang et al. (Wang et al. 2009), in order to incorporate more accurate spatial variation. The reference configuration of the FE model was based on early diastole, where pressure is at a minimum, but the ventricle is still partially loaded. In the future, techniques for determining the unloaded geometry will be incorporated, similar to Krishnamurthy et al. (Krishnamurthy et al. 2013). The strain field that

was calculated from the 3D SPAMM images contained a small amount noise. This was minimized as much as possible by smoothing the strain at each point of interest with the neighboring values. Despite these limitations, the results of the current work are consistent with those of previous studies.

5. Conclusions

The technique presented in the current study was able to determine the in-vivo passive material properties and collagen fiber orientation in a porcine model of myocardial infarction. Additionally, the passive material properties in the remote region were also determined. The results showed that the stiffness in the infarct was higher than the remote region, which is consistent with previous ex-vivo studies. In future work, this technique will be used to assess changes in infarct stiffness and fiber architecture over a serial time course. Very few studies have investigated these types of serial changes, which are critical for understanding the mechanisms that drive remodeling. The ultimate goal is to use this technique in the design of therapies for treating MI.

Acknowledgements

This study was supported by National Institutes of Health grants R01 HL063954 (Gorman), R01 HL111090 (Burdick), and T32 HL007954 (Burdick). The user-defined material subroutine was originally developed under grant R01 HL077921.

Conflict of Interest

None.

References

- Augenstein KF, Cowan BR, LeGrice IJ, Nielsen PM, Young AA (2005) Method and apparatus for soft tissue material parameter estimation using tissue tagged magnetic resonance imaging. *J Biomech Eng* 127:148-157
- Augenstein KF, Cowan BR, LeGrice IJ, Young AA (2006) Estimation of cardiac hyperelastic material properties from mri tissue tagging and diffusion tensor imaging. *Med Image Comput Comput Assist Interv Int Conf Med Image Comput Comput Assist Interv* 9:628-635
- Fomovsky GM, Rouillard AD, Holmes JW (2012) Regional mechanics determine collagen fiber structure in healing myocardial infarcts. *J Mol Cell Cardiol* 52:1083-1090
- Go AS, Mozaffarian D, Roger VL et al (2014) Heart disease and stroke statistics--2014 update: A report from the american heart association. *Circulation* 129:e28-e292
- Guccione JM, McCulloch AD, Waldman LK (1991) Passive material properties of intact ventricular myocardium determined from a cylindrical model. *J Biomech Eng* 113:42-55
- Gupta KB, Ratcliffe MB, Fallert MA, Edmunds LH, Jr., Bogen DK (1994) Changes in passive mechanical stiffness of myocardial tissue with aneurysm formation. *Circulation* 89:2315-2326
- Holmes JW, Borg TK, Covell JW (2005) Structure and mechanics of healing myocardial infarcts. *Annu Rev Biomed Eng* 7:223-253
- Holmes JW, Nunez JA, Covell JW (1997) Functional implications of myocardial scar structure. *Am J Physiol* 272:H2123-2130
- Hooks DA, Trew ML, Caldwell BJ, Sands GB, LeGrice IJ, Smaill BH (2007) Laminar arrangement of ventricular myocytes influences electrical behavior of the heart. *Circ Res* 101:e103-112

Jackson BM, Gorman JH, Moainie SL et al (2002) Extension of borderzone myocardium in postinfarction dilated cardiomyopathy. *J Am Coll Cardiol* 40:1160-1167

Kichula ET, Wang H, Dorsey SM et al (2013) Experimental and computational investigation of altered mechanical properties in myocardium after hydrogel injection. *Ann Biomed Eng*

Krishnamurthy A, Villongco CT, Chuang J et al (2013) Patient-specific models of cardiac biomechanics. *J Comput Phys* 244:4-21

Lee WN, Pernot M, Couade M et al (2012) Mapping myocardial fiber orientation using echocardiography-based shear wave imaging. *IEEE Trans Med Imaging* 31:554-562

Morita M, Eckert CE, Matsuzaki K et al (2011) Modification of infarct material properties limits adverse ventricular remodeling. *Ann Thorac Surg* 92:617-624

Moulton MJ, Creswell LL, Downing SW, Actis RL, Szabo BA, Pasque MK (1996) Myocardial material property determination in the in vivo heart using magnetic resonance imaging. *Int J Card Imaging* 12:153-167

Nair AU, Taggart DG, Vetter FJ (2007) Optimizing cardiac material parameters with a genetic algorithm. *J Biomech* 40:1646-1650

Okamoto RJ, Moulton MJ, Peterson SJ, Li D, Pasque MK, Guccione JM (2000) Epicardial suction: A new approach to mechanical testing of the passive ventricular wall. *J Biomech Eng* 122:479-487

Rouillard AD, Holmes JW (2012) Mechanical regulation of fibroblast migration and collagen remodelling in healing myocardial infarcts. *J Physiol* 590:4585-4602

Stander N, Roux W, Eggleston T, Craig K (2012) Ls-opt user's manual version 4.2.
<http://www.lsoptsupport.com/documents/manuals>.

- Sun K, Stander N, Jhun C-S et al (2009) A computationally efficient formal optimization of regional myocardial contractility in a sheep with left ventricular aneurysm. *J Biomech Eng* 131:111001
- Walker JC, Ratcliffe MB, Zhang P et al (2005) Mri-based finite-element analysis of left ventricular aneurysm. *Am J Physiol Heart Circ Physiol* 289:H692-700
- Wang VY, Lam HI, Ennis DB, Cowan BR, Young AA, Nash MP (2009) Modelling passive diastolic mechanics with quantitative mri of cardiac structure and function. *Med Image Anal* 13:773-784
- Wenk JF, Sun K, Zhang Z et al (2011) Regional left ventricular myocardial contractility and stress in a finite element model of posterobasal myocardial infarction. *J Biomech Eng* 133:044501
- Wenk JF, Zhang Z, Cheng G et al (2010) First finite element model of the left ventricle with mitral valve: Insights into ischemic mitral regurgitation. *Ann Thorac Surg* 89:1546-1553
- Xi J, Lamata P, Niederer S et al (2013) The estimation of patient-specific cardiac diastolic functions from clinical measurements. *Med Image Anal* 17:133-146
- Xu C, Pilla JJ, Isaac G et al (2010) Deformation analysis of 3d tagged cardiac images using an optical flow method. *J Cardiovasc Magn Reson* 12:19
- Zhang S, Crow JA, Yang X et al (2010) The correlation of 3d dt-mri fiber disruption with structural and mechanical degeneration in porcine myocardium. *Ann Biomed Eng* 38:3084-3095

Tables

Table 1: Optimization Parameter Ranges

		Min	Max
Remote	C (kPa)	0.1	10
	b _f	1	100
	b _t	1	50
	b _{fs}	1	50
Infarct	C (kPa)	0.1	25
	b _f	1	250
	b _t	1	60
	b _{fs}	1	60
	epi-angle (deg)	-50	0
	endo-angle (deg)	30	90

Table 2: Optimization Results

		Case				
		1	2	3	4	Avg ± Std
Remote	C (kPa)	1.99	4.89	0.917	0.367	2.04 ± 2.02
	b _f	9.93	8.08	12.49	99.31	32.45 ± 44.61
	b _t	2.32	2.78	6.00	38.87	12.49 ± 17.66
	b _{fs}	46.53	7.77	19.81	4.90	19.75 ± 18.98
Infarct	C (kPa)	0.109	1.01	1.20	1.22	0.88 ± 0.53
	b _f	221.8	182.3	112.3	179.8	174.07 ± 45.47
	b _t	55.53	12.02	11.07	31.72	27.58 ± 20.92
	b _{fs}	48.16	11.79	24.62	25.31	27.47 ± 15.13
	epi-angle (deg)	-49.21	-22.31	-0.45	-0.829	-18.20 ± 23.06
	endo-angle (deg)	43.28	41.31	44.66	41.32	42.65 ± 1.64
	MSE	9.30	9.80	11.62	4.28	8.75 ± 3.14

Figure Captions

Figure 1: Example of coronary artery ligation pattern for case 1. Note that the LV has been opened through the intraventricular septum and “unrolled”. The infarct involves the posterolateral wall of the LV; the anterior and septal walls are spared. Markers bound the infarct region. LAD=left anterior descending artery; D=diagonal branch artery; OM=obtuse marginal branch artery; PD=posterior descending artery; INF=infarct

Figure 2: Short axis view of 3D SPAMM images from case 1 at early diastole with (a) endocardial and (b) epicardial contours, and short axis view at end-diastole with (c) endocardial contour. Short axis view of LGE image at (d) early diastole, with marker circled and boundaries defined.

Figure 3: Pressure vs. time collected from LV catheterization of case 2. The circles indicate the early diastolic and end-diastolic time points.

Figure 4: Finite element models of each infarcted porcine LV for (a) case 1, (b) case 2, (c) case 3, and (d) case 4. The infarcted regions are shown as blue element and the remote as red.

Figure 5: Flowchart of the optimization procedure showing the loop for a single generation.

Figure 6: Optimization results for case 4 depicting two infarct parameters. (a) 3D plot of \mathbf{b}_f versus C with the MSE on the vertical axis. Each point represents a unique design generated by

the optimization. (b) 2D slice of plot (a) with \mathbf{b}_f versus MSE. The converging cluster of points coincides with the red boxed area in (a).

Figure 7: Optimization results by parameter for case 2. The non-angle values in Table 1 were normalized by their respective ranges allowed by the optimization. Results for the remote region can be seen in (a), whereas the infarct results are in (b) with the angles in (c).

Figure 8: Simulated equi-biaxial extension tests of optimized parameters. The values in Table 2 were input into the constitutive equation, and these plots were then generated using an in-house MATLAB script for biaxial testing. The remote results can be seen in (a) and the results from the infarct region in (b).

Figure 9: Average stress-strain curves from simulated equi-biaxial extension testing. For each strain point in Fig. 4, the corresponding stresses of each case were averaged for the remote and infarcted regions, respectively.

Figures

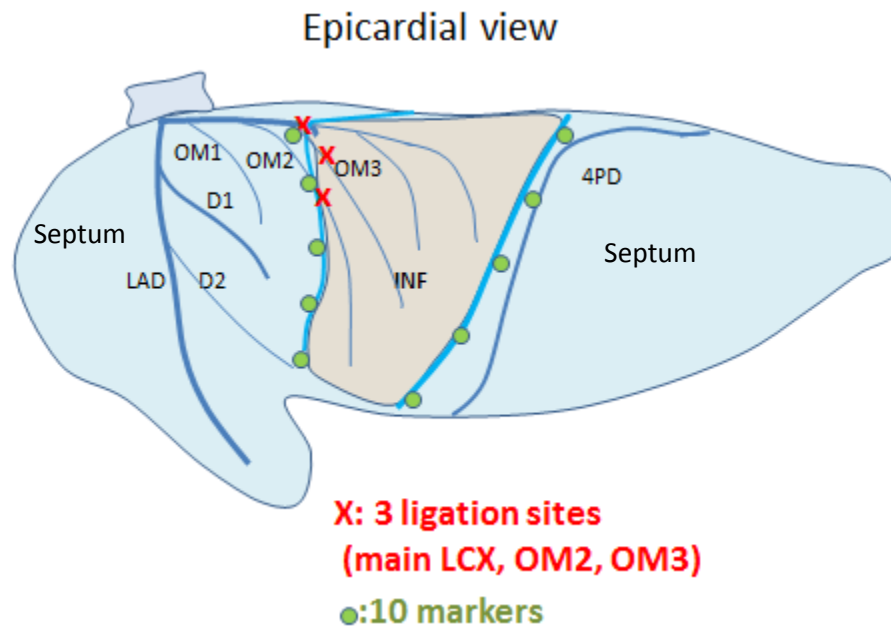
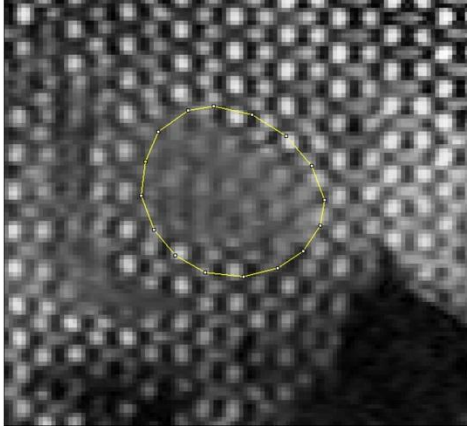
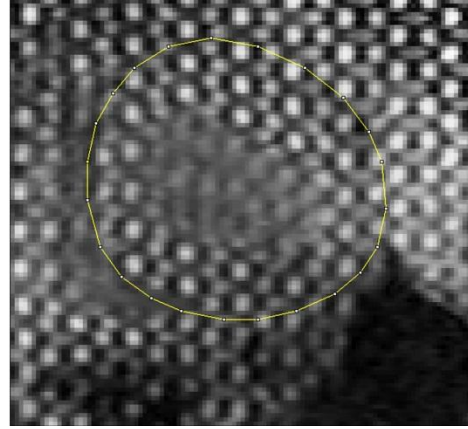


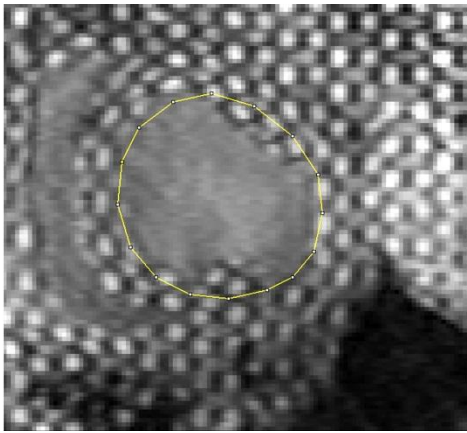
Figure 1: Example of coronary artery ligation pattern for case 1. Note that the LV has been opened through the intraventricular septum and “unrolled”. The infarct involves the posterolateral wall of the LV; the anterior and septal walls are spared. Markers bound the infarct region. LAD=left anterior descending artery; D=diagonal branch artery; OM=obtuse marginal branch artery; PD=posterior descending artery; INF=infarct



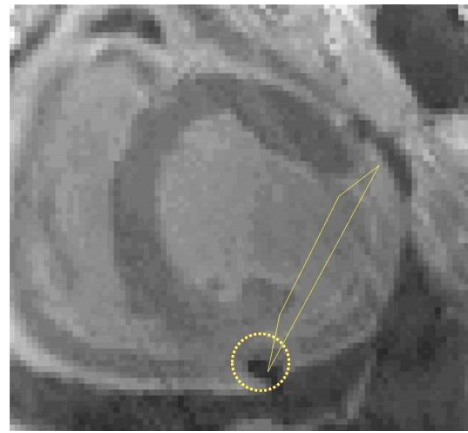
(a)



(b)



(c)



(d)

Figure 2: Short axis view of 3D SPAMM images from case 1 at early diastole with (a) endocardial and (b) epicardial contours, and short axis view at end-diastole with (c) endocardial contour. Short axis view of LGE image at (d) early diastole, with marker circled and boundaries defined.

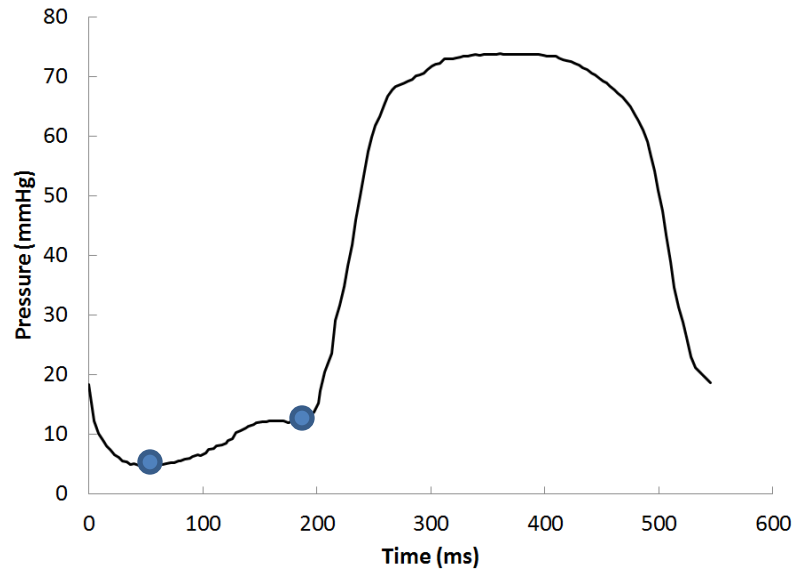


Figure 3: Pressure vs. time collected from LV catheterization of case 2. The circles indicate the early diastolic and end-diastolic time points.

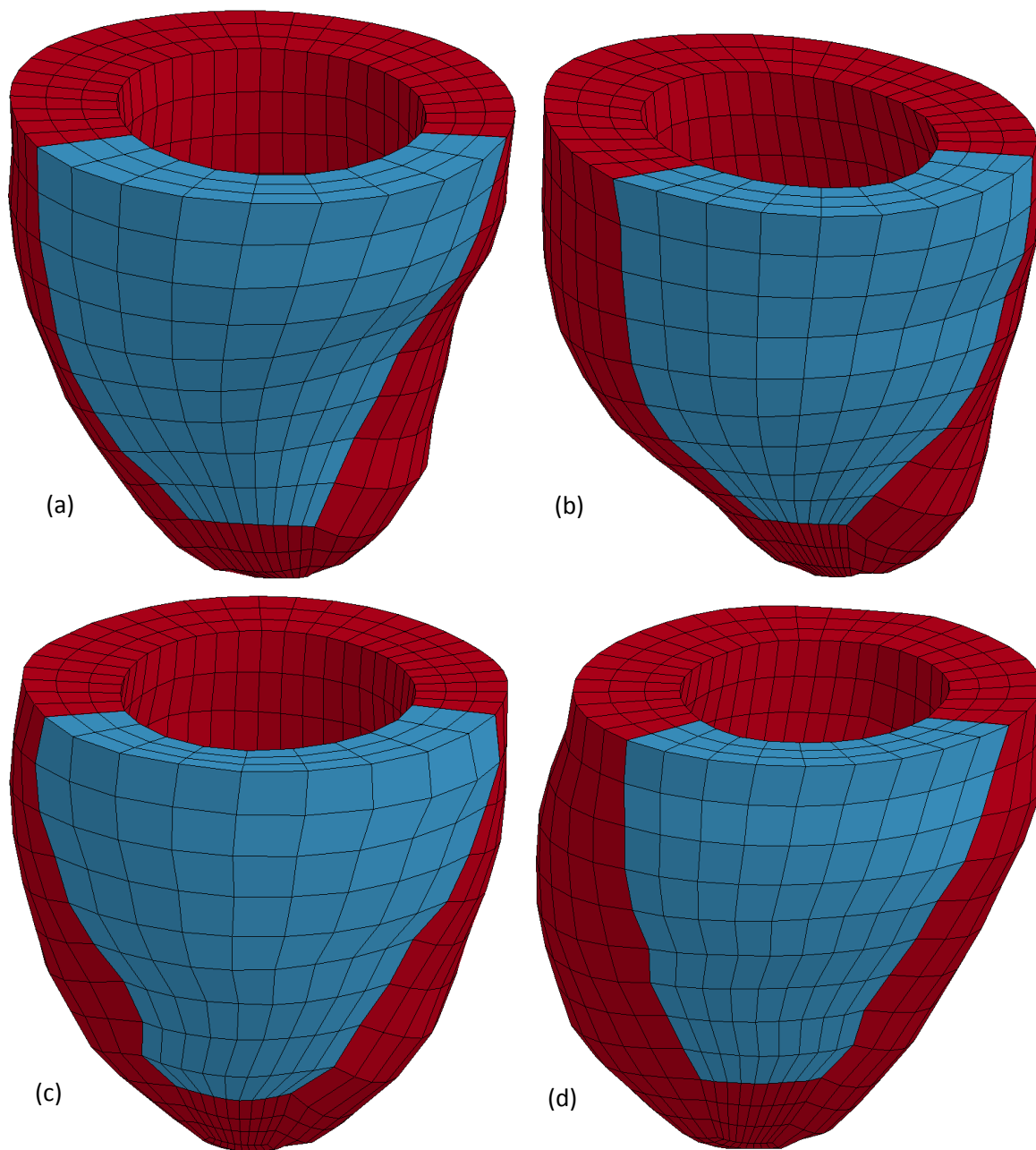


Figure 4: Finite element models of each infarcted porcine LV for (a) case 1, (b) case 2, (c) case 3, and (d) case 4. The infarcted regions are shown as blue element and the remote as red.

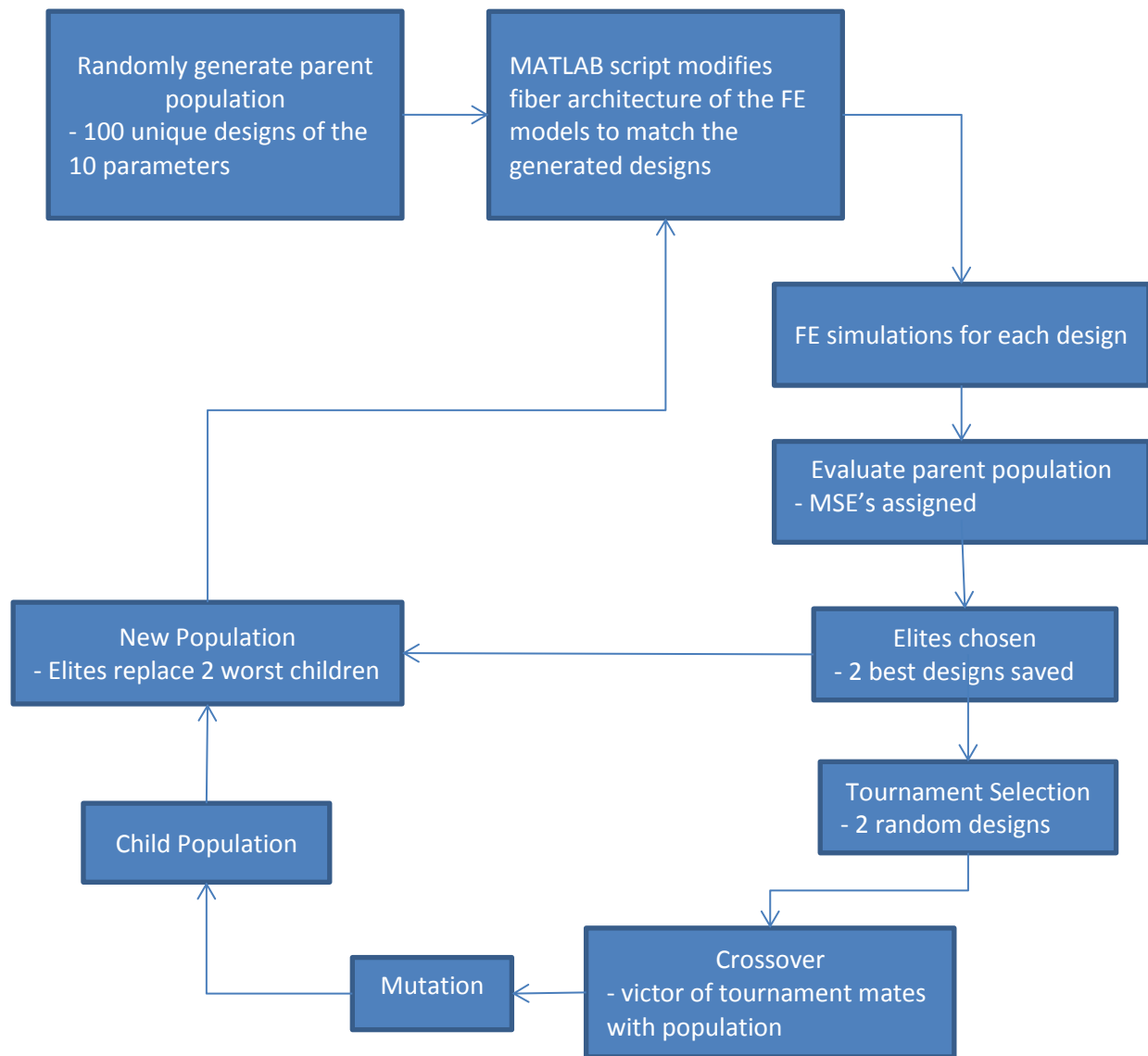


Figure 5: Flowchart of the optimization procedure showing the loop for a single generation.

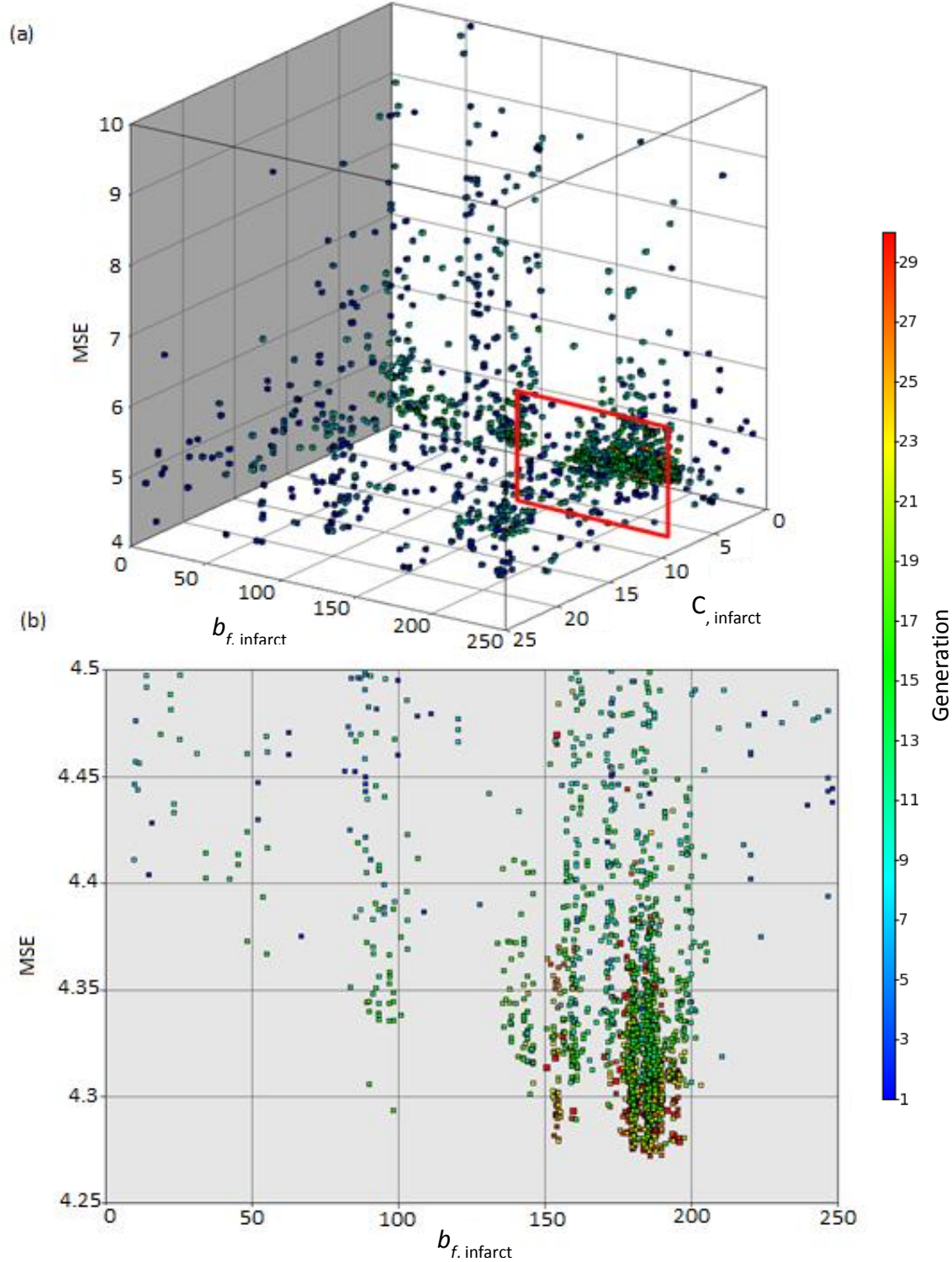


Figure 6: Optimization results for case 4 depicting two infarct parameters. (a) 3D plot of \mathbf{b}_f versus C with the MSE on the vertical axis. Each point represents a unique design generated by the optimization. (b) 2D slice of plot (a) with \mathbf{b}_f versus MSE. The converging cluster of points coincides with the red boxed area in (a).

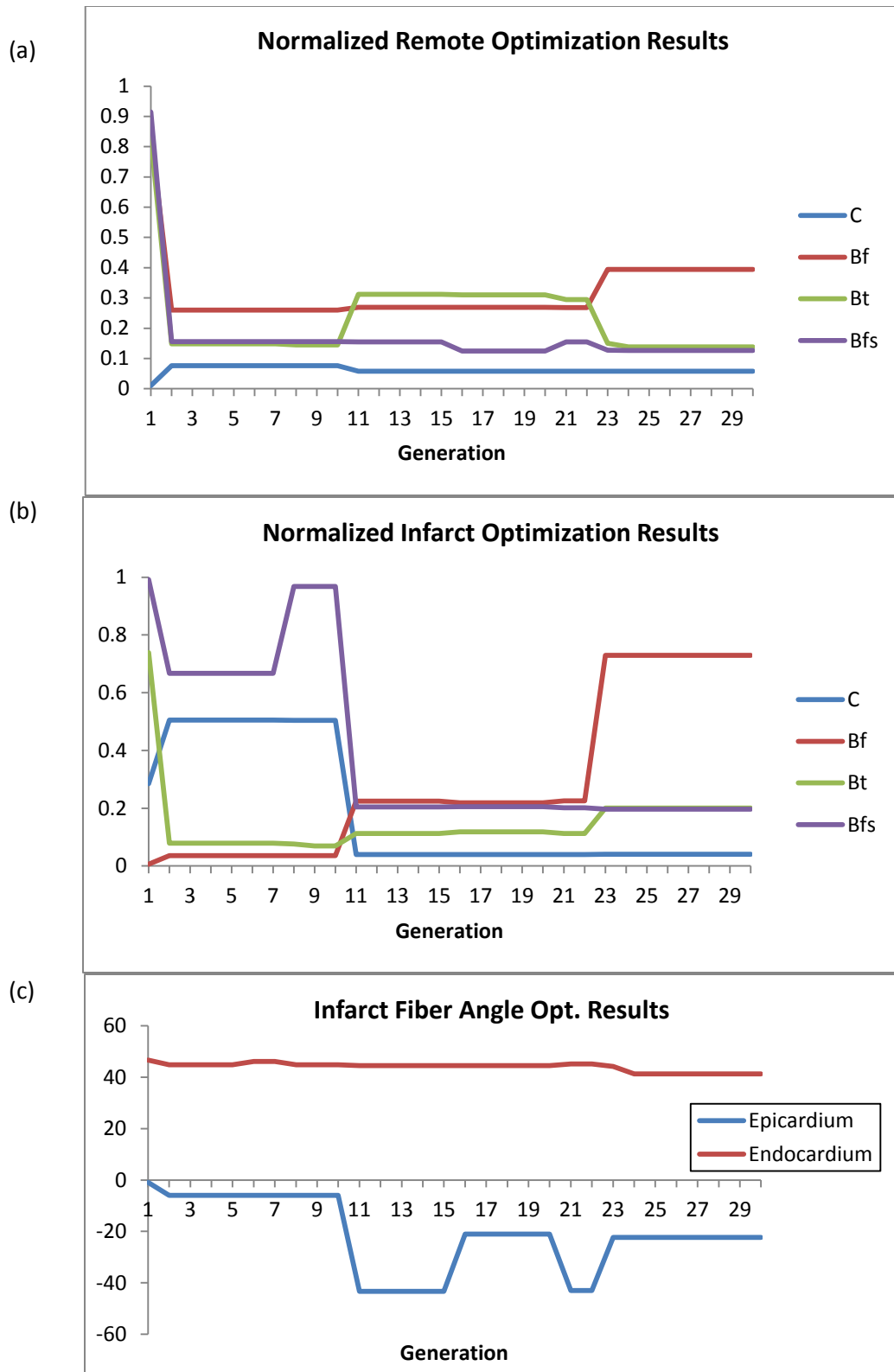


Figure 7: Optimization results by parameter for case 2. The non-angle values in Table 1 were normalized by their respective ranges allowed by the optimization. Results for the remote region can be seen in (a), whereas the infarct results are in (b) with the angles in (c).

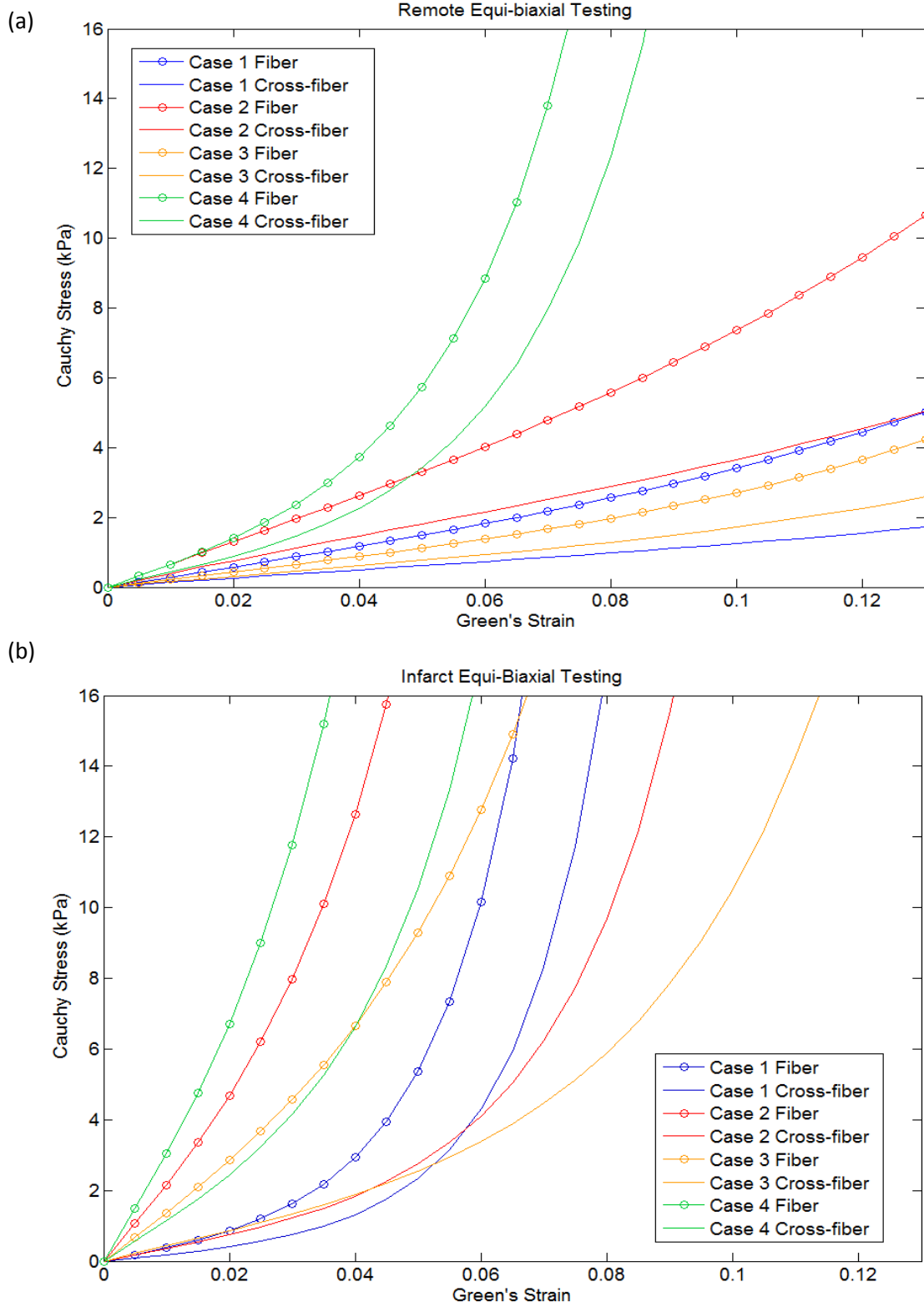


Figure 8: Simulated equi-biaxial extension tests of optimized parameters. The values in Table 2 were input into the constitutive equation, and these plots were then generated using an in-house MATLAB script for biaxial testing. The remote results can be seen in (a) and the results from the infarct region in (b).

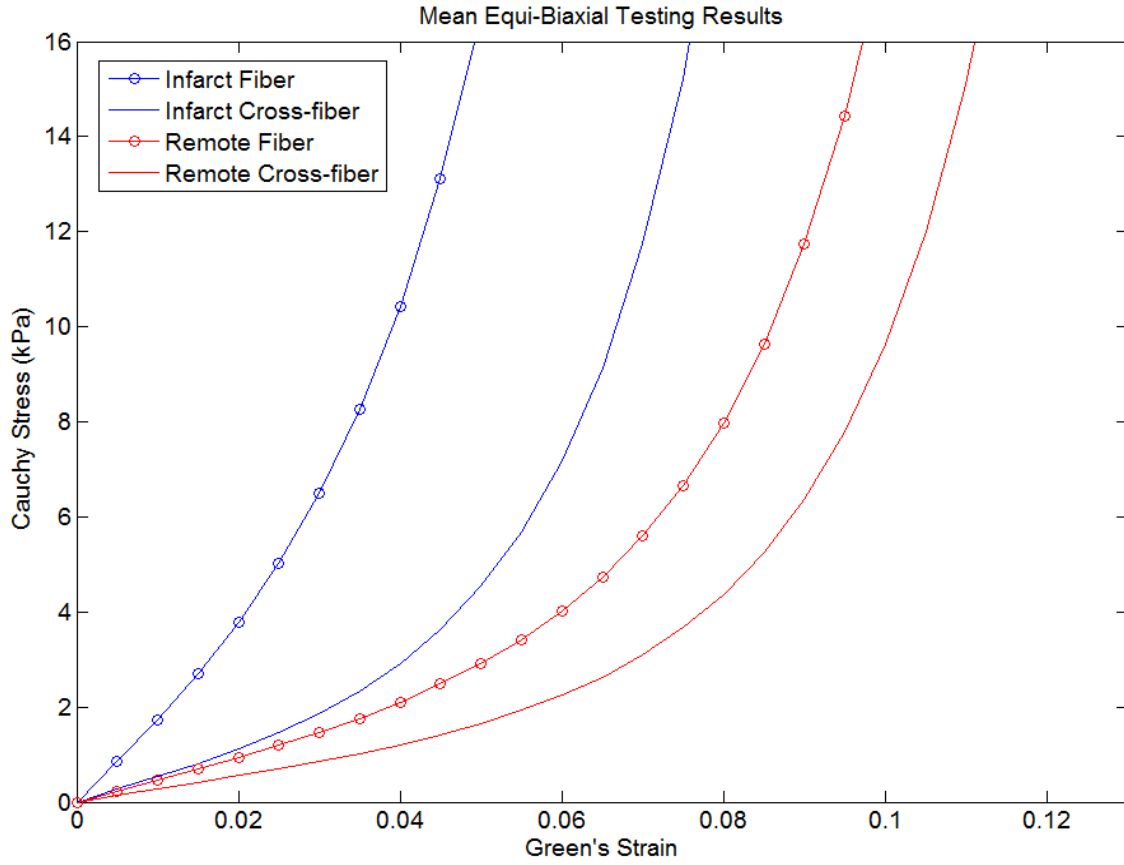


Figure 9: Average stress-strain curves from simulated equi-biaxial extension testing. For each strain point in Fig. 4, the corresponding stresses of each case were averaged for the remote and infarcted regions, respectively.